# Embedded WMLES of shock boundary-layer interaction on a nacelle-aircraft configuration

Marius Herr* and Axel Probst†
*German Aerospace Center, Göttingen, Germany, 37073*

Sebastian Spinner‡ and Ralf Rudnik§
*German Aerospace Center, Braunschweig, Germany, 38108*

Rolf Radespiel¶
*Technische Universität Braunschweig, Germany, 38108*

**Research on a long-range transport aircraft with ultra-high bypass ratio (UHBR) nacelles at transonic flow conditions is presented. In this context, different numerical as well as experimental methodologies are employed. A major research issue is the aerodynamic interaction of the flow field with the UHBR nacelle, pylon, fuselage and wing lower side at negative angles of attack. The interactions of transonic shocks with the boundary layer are analysed by Reynolds-averaged Navier-Stokes (RANS) simulations with regard to flow separation and recirculation. Further investigations are performed for a transonic shock on the outside of the nacelle with turbulence resolving simulation approaches. For this purpose, two embedded wall-modelled large eddy simulation (WMLES) methods based on different RANS background models (Menter's shear stress transport model (SST) and Reynolds stress equation model (RSM)) in combination with a synthetic turbulence generator (STG) are employed. This allows to analyse the dynamics of the shock front with regard to shock buffet. The results are compared to experimental data of pressure sensors, unsteady pressure sensitive paint (unsteady PSP) and particle image velocimetry (PIV) measurements obtained in wind tunnel testing at the European Transonic Windtunnel (ETW). Furthermore, the impact of the angle of attack on the shock boundary-layer interaction is evaluated. The numerical and experimental data show consistent results in terms of shock positions and shock dynamics.**

## I. Nomenclature

---

Presented as Paper 2023-0246 at the AIAA SCITECH 2023 Forum, National Harbor, MD, 23-27 January 2023

[*] Research Scientist, Institute of Aerodynamics and Flow Technology, $C^2A^2S^2E$; marius.herr@dlr.de (Corresponding Author).

[†] Team Lead, Institute of Aerodynamics and Flow Technology, $C^2A^2S^2E$.

[‡] Research Scientist, Institute of Aerodynamics and Flow Technology, Transport Aircraft Devision.

[§] Head of Department, Institute of Aerodynamics and Flow Technology, Transport Aircraft Devision.

[¶] Professor (Retired), Institute of Fluid Mechanics.

$\underline{\vec{A}}$ = Cholesky decomposition of Reynolds stress tensor

$\alpha$ = angle of attack

$\alpha_g$ = geometrical function in WMLES blending function

c = local chord length

$C_{DES}$ = calibration constant

$c_f$ = skin friction coefficient

$\overline{c_i}$ = time averaged coefficient $c_i$

$\langle c_i \rangle$ = spatially averaged coefficient $c_i$

$c_p$ = pressure coefficient

$\vec{d}$ = directional vector

$d_r$ = extension of refinement region in r-direction

$d_w$ = local wall distance

$\delta$ = boundary-layer thickness

$\Delta_{DES}$ = function of grid spacing in DES method

$\Delta t$ = time step size

$\Delta d$ = thickness

$f_B$ = WMLES blending function

$f_{dt}$ = IDDES delaying function

$f_e$ = WMLES model function

$\Gamma$ = region of local flow separation

$h_{max}$ = maximum local edge length

$k$ = wave number

$l_{LES}$ = LES length scale

$l_{RANS}$ = RANS length scale

$l_{WMLES}$ = WMLES length scale

Ma = Mach number

$\mu$ = dynamic viscosity

N = number of Fourier modes

n = running index

$\Omega$ = WMLES region

$\phi$ = mode phase

$\varphi$ = circumferential coordinate

$q$ = normalized mode amplitudes

$r$ = radius

$\vec{r}$ = position vector

Re = Reynolds number

$\mathrm{Re}_\tau$ = Reynolds number with regard to wall shear stress

$\rho$ = mass density

$s$ = mode frequency

$\sigma$ = standard deviation

$\vec{\sigma}$ = directional vector

$t$ = time

$\tau$ = time scale

$\tilde{\vec{u}}'$ = unscaled injected velocity fluctuation vector by STG

$\vec{u}'_{ST}$ = injected velocity fluctuation vector by STG

$\overline{U_{\mathrm{inf}}}$ = time averaged farfield velocity

$\overline{u_x}$ = time averaged x-velocity

$x$ = $x$-coordinate

$x_s$ = location of shock front in x-direction

$x_{STG}$ = location of STG in x-direction

$y$ = $y$-coordinate

$y^+$ = non-dimensional wall distance

$z$ = $z$-coordinate

$\zeta$ = coordinate direction

# II. Introduction

Aircraft configurations at transonic flow conditions are exposed to locally occurring supersonic flow regions. These regions, which mostly occur on the wing surface, are closed off by transonic shocks and thus transformed into subsonic flows. Depending on the strength of the shock, which is influenced by the flight Mach number and the angle of attack, a strong interaction with the local turbulent boundary layer may arise potentially leading to flow separation. This phenomenon is also referred to as a high-speed stall, which occurs when the aircraft is operated at the high-speed border of its flight envelope [1] . Additionally, shock boundary-layer interaction can exhibit an oscillatory shock motion on the wing surface, which is also known as shock buffet. This buffet phenomenon may cause dangerous flight conditions and is important to avoid from a safety-related perspective. A further level of complexity arises in commercial transport aircraft configurations coupled with UHBR engines at transonic flow conditions. Depending on the Mach number and angle of attack, the engine integration can lead to local flow accelerations, enhancing local shock boundary-layer interaction, which possibly result in shock buffet. On top of that, these interactions may also arise on the outer curved surfaces of the engine nacelles.

The scientific literature on such engine-integration effects mainly contains studies on the transonic flow behaviour at cruise conditions [2–4]. However, in the area of high-speed stall, i.e. at off-design conditions, there are only few studies with either simplified wing segment-nacelle configurations [5, 6] or in which the integration of the engine is not in focus [7]. Apart from [8, 9], there are, to the authors' knowledge, neither experimental nor numerical studies available for a complete and realistic aircraft configuration with regard to engine integration at high-speed off-design conditions. Significantly more studies on the transonic shock buffet and shock boundary-layer interaction are available, if it only occurs on the wing upper surface and the engine integration plays no or only a subordinate role. For example, various experimental studies were carried out on a 3-D swept wing in [10–12] as well as on the NASA common research model (CRM) in [13, 14]. In the area of numerical investigations, studies using turbulence-resolving methods are particularly noteworthy. For instance, in [15, 16] the detached delayed eddy simulation (DDES) method coupled with the Spalart-Allmaras Reynolds-averaged Navier-Stokes (SA-RANS) turbulence model was applied on the RBC12 wing-body half model at transonic flow conditions and good agreements with experimental data were reported. In a further study, the automated zonal detached eddy simulation (AZDES) and the SA-DDES methodology were used to investigate the shock buffet at the NASA CRM and reliable predictions of the buffet behaviour were achieved [17]. In a more recent study [7], the authors investigate the upper-wing buffet occurring at the Boeing transonic truss-braced wing aircraft (TTBW) with the zonal detached eddy simulation (SA-ZDES). Furthermore, WMLES results of the entire NASA CRM configuration were presented in several publications analysing wing buffet effects [18–20]. With regard to the transonic effects of the external flows around engine nacelles, there are a few studies that examine isolated through flow nacelles. In an early study, a long duct nacelle was analysed with a two equation RANS model and in particular the drag increase due to transonic shocks was evaluated [21]. In a recent study, experimental and numerical methods (SST-RANS) were used to investigate optimised high bypass ratio (HBR) engines which achieved consistent results with regard to the shock position [22].

This study deals with a long-range wide-body transport aircraft configuration (XRF1) designed by Airbus with modern UHBR nacelles at transonic flow conditions and negative angles of attack. The large diameter of the nacelle requires a close coupling between the nacelle and the wing. This leads to the formation of channel-like flow regions with a narrowing cross-section and thus with local flow acceleration [8]. On the one hand, such channels arise in the space between the nacelle, pylon and wing lower side. On a larger scale, a further semi-open channel occurs, consisting of nacelle, pylon, lower wing surface and fuselage. For negative angles of attack, transonic shocks within these channels are expected to be enhanced by the accelerated flow, which possibly leads to strong shock boundary-layer interaction. Therefore, this paper analyses these interactions occurring in the described channel regions with regard to shock strengths, flow separation and the formation of areas of recirculation (AOR) with a turbulence modelling approach. Due to the negative angle of attack, a further transonic shock arises outside of the semi-open channel on the outside of the UHBR nacelle, which is thoroughly investigated in this paper. The dynamics of this shock is analysed using turbulence resolving numerical as well as time resolved experimental methods and it is examined whether shock buffet occurs in this flow region. Furthermore, the dependence of the shock behaviour on the angle of attack is investigated. Thus, contrary to [21, 22], where only isolated nacelles were examined, interference effects from wing, pylon and body are taken into account here, providing realistic flow conditions for the nacelle flow. Note that the present study is directly related to the work of Spinner et. al [9], who investigated the aforementioned semi-open channel of the same XRF1-UHBR configuration at identical flow conditions using a turbulence resolving method and demonstrated excellent agreement with experimental data. However, the remaining area, including the outside of the nacelle, was treated with a turbulence modelling approach (RANS), so that this study virtually represents a complementary investigation to [9]. The investigations presented here are part of the research unit FOR 2895, funded by the German Research Foundation (DFG), which deals with the flow phenomenon of high-speed stall on commercial aircraft configurations [1]. This research initiative is characterised in particular by extensive measurement campaigns, which were carried out over a large range of Reynolds numbers with unsteady PSP and time-resolved PIV at cryogenic measurement conditions in the ETW [23–27]. The investigated XRF1 wind tunnel model provided by Airbus was previously equipped with a UHBR flow-through nacelle designed by the German Aerospace Center (DLR) [28]. An important finding of a measurement campaign was that the lower wing buffet arises for very low angle of attack at high subsonic Mach numbers and is visible over a large range of Reynolds numbers motivating the herein used flow conditions [8]. Another important element of the research unit is the further development and application of hybrid RANS - large eddy simulation (LES) methods to the high-speed stall phenomenon.

A common approach to simulate unsteady flow phenomena at aircraft configurations is the use of unsteady RANS (URANS) methods. However, as mentioned for example in [29], even sophisticated Reynolds stress based URANS models have weaknesses in describing the dynamics of separated boundary layer flows and its aerodynamical effects (e.g. airfoil lift coefficients at high angles of attack). Because of this, a turbulence resolving simulation method seems necessary for describing the highly unsteady physics of complex shock boundary-layer interaction. Since the fully scale resolving direct numerical simulation (DNS) method is still restricted to low Reynolds number flows, the LES method might generally be suitable for this study. The herein used Reynolds number, however, does not allow to resolve the entire flow field up to the micro scales of near-wall turbulence. Instead, a combination of LES for resolving complex physical phenomena and classical RANS modelling for near-wall turbulence (WMLES) is a potential remedy to obtain accurate results with reasonable amount of computing resources. A prominent representative of such a hybridisation of RANS and LES is the improved delayed detached eddy simulation (IDDES) method [30], which includes a WMLES functionality and is also used in this work. To conduct the intended investigations of the lower wing buffet with complex corner flows as accurately as possible, the IDDES methodology was coupled to the Speziale-Sarkar-Gatski / Launder-Reece-Rodi (SSG/LRR) RSM as outlined in detail in [31]. An RSM is particularly suitable for capturing the secondary flows occurring in the intersection regions between pylon and lower wing as well as pylon and nacelle because, contrary to eddy viscosity models, it allows to capture turbulence anisotropy. To further validate this newly developed methodology, it is also used in this work to analyse the transonic shock on the nacelle and compared to the well established SST-WMLES. The RSM-WMLES mode of IDDES is thereby applied locally to the lower nacelle, such that the surrounding flow is treated in RSM-RANS mode which is referred to as embedded WMLES.

This study is organised as follows. The description of the employed methods and the computational grids is given in Sec. III. In Sec. IV.A, SST-RANS investigations on flow effects on the lower wing side, which are attributable to the engine integration, are presented. This is followed by Sec. IV.B with detailed investigations on the transonic shock on the lower side of the nacelle with SST-WMLES results and comparisons to experimental data from pressure taps, unsteady PSP and PIV measurements. In Sec. IV.C, it is analysed to what extent a steepening of the angle of attack affects the shock at the nacelle, additionally using the RSM-WMLES methodology. The paper concludes with a summary of the results and a brief outlook in Sec. V.

## III. Model, methods and numerical setups

### A. Model description

The XRF1 is a research configuration designed by Airbus representative of a state of the art wide-body long-range transport aircraft. A corresponding wind tunnel model (Fig. 1) was provided to the research unit (FOR 2895) to assess the flow phenomena at high-speed off-design conditions. The existing Very-High-Bypass-Ratio nacelles were replaced by a new UHBR through flow nacelle design for the wind tunnel model [28]. The design pursued the goal to provide a test case for high-speed stall phenomena related to UHBR integration effects while maintaining representative performance under cruise conditions. The nacelle is composed of multiple parts featuring an outer casing, a core body and a plug inside the core body in order to achieve comparable displacements effects with real engine flows. In addition a new pylon was designed as well to account for the increase in nacelle size and weight. The outer nacelle shape is realized as a circular casing with airfoil-like cross-section although it is not rotationally symmetric due to the introduction of a 3° inlet droop. For more details on the design of the UHBR through flow nacelle the reader is referred to [28].

### B. Flow Solver

The DLR TAU code is employed to perform the presented statistical RANS as well as scale resolving WMLES simulations. TAU is a compressible flow solver using an unstructured finite volume method which is applicable for

Fig. 1 Long-range transport aircraft configuration (XRF1) with UHBR-nacelles.

Table 1 Overview of simulation runs with respect to the employed computing resources.

| Simulation | # time steps | # inner iteration / time step | runtime / days | # cores | core hours / $10^6$ |
|---|---|---|---|---|---|
| SST-RANS (refined mesh) | - | - | 2.4 | 768 | 0.044 |
| RSM-RANS (refined mesh) | - | - | 4.1 | 768 | 0.075 |
| SST-WMLES (-4.0°) | 80000 | 30.5 | 43.3 | 1824 | 1.895 |
| SST-WMLES (-4.5°) | 80000 | 30.6 | 38.8 | 2112 | 1.968 |
| RSM-WMLES (-4.5 °) | 80000 | 32.6 | 68.3 | 2400 | 3.933 |

hybrid meshes with structured and unstructured areas [32]. Both methods employ a second order central scheme for the discretization of convective fluxes which uses the skew symmetric convection operator by Kok [33] in conjunction with a matrix-dissipation operator [34]. Additionally, for the WMLES simulations a hybrid low-dissipation low-dispersion scheme (HLD2) [35] is used to ensure high numerical accuracy in the areas with resolved turbulence. With regard to the temporal discretization for WMLES an implicit dual time stepping approach of second order accuracy is applied. In addition, Cauchy-convergence criteria are employed for the inner time iterations and used for relevant integral flow quantities (lift-, drag- and side force coefficient). The average number of inner iterations per time step is given in Tab.1 for each simulation run. For the RANS turbulence model as well as for the RANS background model of WMLES two different turbulence models are used, namely, the SST two-equation model [36] and the SSG/LRR RSM [29]. Table 1 provides an overview of the employed computing resources and wall-clock runtimes of the presented simulations. Note, however, that the RSM-WMLES was performed on two different HPC systems (cf. Acknowledgments).

### C. RANS mesh

A hexa-dominant unstructured mesh was created to resolve the flow around the XRF1-UHBR half model in free air condition. Special care was taken on the resolution of boundary layer flow by ensuring a $y^+$ below 0.4 and selecting a wall normal growth rate of 1.12. An estimate of the boundary-layer thickness was used along with a safety factor of 2 to

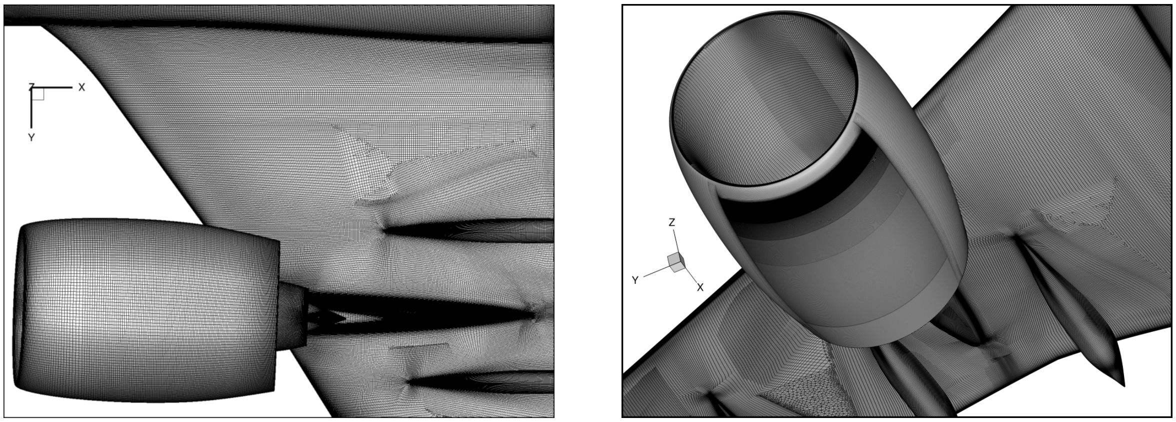

**(a) Nacelle and wing inboard area, view from below**

**(b) Nacelle, view from front below**

**Fig. 2 Features of the XRF1 surface mesh around the region of interest before and after refinement for WMLES.**

estimate the required stack height of prism layer close to the surface. Wherever possible an H-type mesh topology was applied in the boundary layer mesh to accurately resolve flow features at surface intersections. The final RANS mesh before LES refinement comprises a total of 112 million points. Details of the surface mesh at and around the nacelle are shown in Fig. 2.

### D. Embedded WMLES method and numerical setup

#### *1. WMLES branch of IDDES and integration to simulation setup*

To effectively perform scale resolving simulations at high Reynolds numbers a hybrid RANS-LES method is used which models the effect of small near-wall eddies (RANS region) while larger eddies in detached flow are resolved (LES region). Therefore the DES-based, non-zonal IDDES methodology by Shur et al. [30], which automatically switches between areas of RANS or LES modelling, is employed. It is used in conjunction with two different RANS models providing the subscale modelling in the LES regions as well as the turbulence modelling in the RANS regions. Both, the widely used SST-IDDES method [37] as well as the novel RSM-IDDES [31] are applied in this study. In the present used simulation setup the WMLES branch of IDDES is enforced by setting the IDDES delaying function to a constant value ($f_{dt} = 1$).

Compared to the DDES branch of IDDES the WMLES functionality only models the inner part of the boundary layer resulting in a reduction of model complexity. The switch between RANS and LES is accomplished through a replacement of the integral length scale $l_{\mathrm{RANS}}$ of the RANS model. Using WMLES this length scale is replaced by $l_{\mathrm{WMLES}}$:

$$l_{\mathrm{WMLES}} = f_B(1 + f_e)l_{\mathrm{RANS}} + (1 - f_B)l_{\mathrm{LES}}, \tag{1}$$

$f_B$ and $f_e$ represent model functions and $l_{\mathrm{LES}}$ is the LES length scale. The blending function $f_B$ solely depends on geometrical sizes $d_w$ and $h_{\max}$ representing the local wall distance and maximal local edge length respectively (cf. Eq. 2).

$$f_B = \min\{2\exp(-9{\alpha_g}^2), 1.0\}, \quad \alpha_g = 0.25 - d_w/h_{\max} \tag{2}$$

Due to this design of $f_B$ , $l_{\text{WMLES}}$ becomes close to $l_{\text{RANS}}$ in near-wall regions and $l_{\text{LES}}$ in the remaining region. The LES length scale is defined as

$$l_{\text{LES}} \propto C_{\text{DES}}\Delta_{\text{DES}} \tag{3}$$

where $C_{\text{DES}}$ is a RANS-model dependent calibration constant and $\Delta_{\text{DES}}$ a function of $h_{\max}$ and $d_w$. Having this definition of $l_{\text{LES}}$ it can be shown that the RANS-model acts similar to the LES model by Smagorinsky [38] and thus a hybridisation of RANS and LES modelling is achieved.

In order to apply the hybrid RANS-LES locally and model the surrounding area with a RANS approach, a desired volume $\Omega$ is specified manually. Therefore the integral length scale $l$ is set to $l_{\text{RANS}}$ outside of $\Omega$ and $l_{\text{WMLES}}$ within $\Omega$. At the RANS-LES interface in flow direction a STG (cf. Sec. III.D.3) is employed. This approach is also referred to as embedded WMLES.

### 2. *Mesh refinement for WMLES*

A cylindrical coordinate system ($r$, $\varphi$ and $x/c$) is used to refer to the nacelle outer surface in a simple and unique manner. Its reference point ($r = 0$) is defined as the center of the nacelle cross section at $x/c = 0$ such that $r$ is nearly constant at the leading edge. $\varphi$ is set to 0° at the center of the interface between pylon and nacelle surface and increasing in clockwise direction such that $\varphi = 90°$ points towards the fuselage.

In order to resolve the dynamics of the transonic shock at the lower nacelle surface a refinement area is defined. This area covers all flow regions directly related to the shock such as the AOR as well as attached and separated boundary layer flow upstream and downstream of the AOR. According to the SST-RANS solution in Fig. 7a this region covers an $x$-range starting from $x/c = 0.06$ to $x/c = 1$ and a $\varphi$-range starting from $\varphi = 120°$ to $\varphi = 225°$ (cf. also Fig. 2b). The extension of the refinement region in $r$-direction ($d_r$) locally depends on the boundary-layer thickness $\delta$ such that $d_r = 1.2\,\delta$. The entire refinement region is surrounded by unstructured blocks in all coordinate directions consisting of prisms and tetrahedrons. This allows to preserve the design and resolution of the outer RANS mesh.

The maximum cell resolution in each coordinate direction $\zeta$ is limited to $\Delta\zeta \leq \delta/10$ and therefore depends on the local boundary-layer thickness $\delta(x)$. For $\Delta x$ and $\Delta r$, this limitation fulfills the commonly used resolution criteria for WMLES [30, 39]. Concerning the circumferential direction, however, the employed boundary ($r\Delta\varphi \leq \delta/10$) might be somewhat too high. Nevertheless, we decided in favour of a more applicable value, due to the enormous additional grid size that would result from a more common resolution criterion ($r\Delta\varphi \leq \delta/20$). Applying $\Delta\zeta \leq \delta/10$ to the refinement region, results in a continuous increase of $\Delta x$ in streamwise direction. This in turn, leads to a total number of 1350 points between trailing and leading edge of the nacelle. In $\varphi$-direction the limitation of $r\Delta\varphi \leq \delta/10$ is realized in a discrete manner and increases stepwise in streamwise direction. Therefore the surface mesh is separated into several subzones (cf. Fig. 2b). The total number of points in lateral direction within these subzones decreases from 4350 points (most upstream) to 250 points (most downstream). The wall normal spacing begins with $\Delta r^{+}(1) = 0.4$ and grows geometrically ($\Delta r(i) = 1.12\Delta r(i-1)$) until $\Delta r = \Delta x$ until is reached. $\Delta r$ is kept constant afterwards to fulfil the isotropy constraint (cf. [40]). Applying this protocol within the refinement height ($d_r = 1.2\,\delta$) the number of grid points in wall normal direction increases from 113 points ($x/c = 0.06$) to 258 points at the trailing edge.

Finally, the total grid number of the WMLES region and the surrounding RANS mesh comprises 420 million grid points. For a more detailed description of the employed mesh the reader is referred to [41].

### *3. Synthetic Turbulence Generator*

At the RANS-LES interface in flow direction at $x_{STG}/c = 0.08$ STG by Adamian and Travin [42] is employed to enforce the transition from modelled to resolved turbulence on the lower side of the nacelle. The STG injects velocity fluctuations which consist of a superposition of $N$ Fourier modes:

$$\vec{u}'_{ST} = \underline{\vec{A}} \cdot \tilde{\vec{u}}'(\vec{r}, t) = \underline{\vec{A}} \cdot \sqrt{6} \sum_{n=1}^{N} \sqrt{q^n} \left[ \vec{\sigma}^n \cos\left( k^n \vec{d}^n \cdot \vec{r}' + \phi^n + s^n \frac{t'}{\tau} \right) \right] \quad . \tag{4}$$

The fluctuations $\tilde{\vec{u}}'$ are calculated from random quantities as well as statistical quantities originating from a local RANS Reynolds stress tensor. The random quantities consist of the mode direction vectors $\vec{d}^n$ and $\vec{\sigma}^n \perp \vec{d}^n$, the mode phase $\phi^n$ and the mode frequency $s^n$. Note that an identical set of these random quantities (same number and values) was used for all simulations with the STG. Regarding the input RANS Reynolds stress tensor which is extracted directly upstream of the RANS-LES boundary a Cholesky decomposition is applied generating the matrix $\underline{\vec{A}}$. The length scale of the extracted RANS data determines the range of the wave number $k^n$. The spectrum of the normalized mode amplitudes $q^n$ is based on the von Kármán model.

For more details regarding the injection of synthetic velocity fluctuations in TAU as well as additional modifications for the application of the STG in volumes the reader is referred to [43]. Further investigations of the STG of the herein presented flow configuration with regard to the positioning of the RANS-LES interface are presented in [41].

# IV. Results

## A. RANS investigations of the entire nacelle-aircraft configuration

During the design phase of the UHBR nacelle parametric studies were conducted in order to assess different off-design flow conditions [28]. In their work, the authors used an unstructured grid with a cell size of 40 million points and performed RANS simulations at a Reynolds number of 25 million using the SA-negative model [44] and the

SSG/LRR-ln($\omega$) Reynolds stress model [29] for turbulence modelling. Although these simulations were performed on a fairly coarse grid they allowed for a thorough assessment of the expected flow behaviour associated with different parameter changes. The key driver for shock-induced separation on the wing lower side and nacelle was found to be lowering the angle of attack. For an inflow Mach number of 0.84 and an angle of attack of $-4\,^\circ$ shock-induced separation could be found on the wing lower side, the pylon and the nacelle.

In this section, the model aerodynamics at these conditions is explained in detail based on simulations to the initial design study. The hexa-dominant mesh described in section IV.A was used to perform steady RANS simulations using the SST turbulence model by Menter [36]. Contrary to the design study [28], these simulations were performed at a smaller Reynolds number of 3.3 million as they were used to prepare the WMLES presented in section IV.B. Figure 3 gives an overview of the resulting surface pressure distribution on the wing, pylon and nacelle. In addition, areas of local flow separation are marked by solid and dashed lines. Solid lines hereby represent lines of $c_f = 0$ and dashed lines indicate negative $c_f$. Due to the low angle of attack of $-4\,^\circ$ strong shocks form on the lower surfaces of wing and nacelle (see Fig. 3a). The inboard area of the wing between nacelle and fuselage is thereby dominated by an $s$-shaped shock that extends even below the fuselage. From this shock a large flow separation originates extending downstream up to the trailing edge and enveloping the inboard flap track fairing. The unsteady interactions of this shock with this flow separation is hereafter described as *UHBR induced buffet on the wing lower surface*. Further analysis of the phenomenon based on experimental and numerical data can be obtained from [8] and [9].

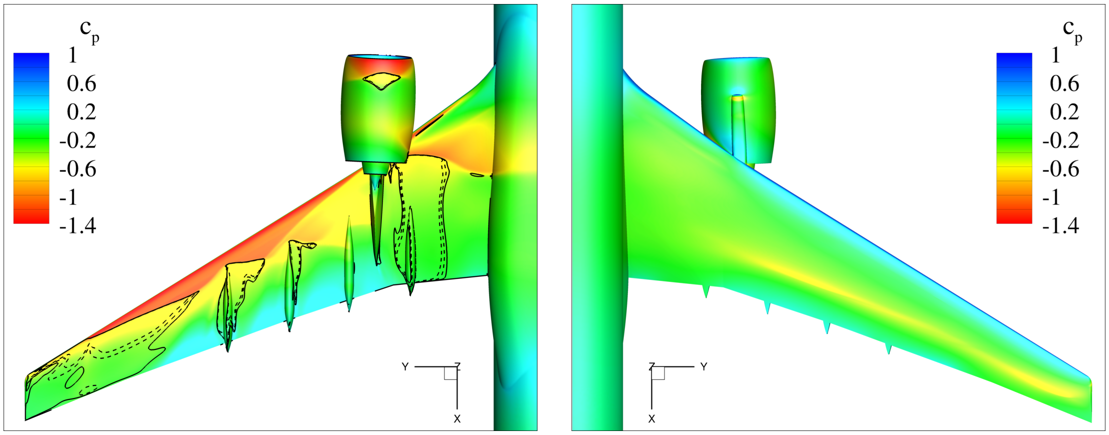

**(a) Wing lower surface** **(b) Wing upper surface**

**Fig. 3 Visualization of wing and nacelle flow at Re = 3.3 million, Ma = 0.84 and $\alpha = -4\,^\circ$. Surface contour represents pressure coefficient, solid lines indicate $c_f = 0$, dashed lines indicate $c_f < 0$.**

Outboard of the nacelle/pylon station the shock front on the wing lower surface is strongly influenced by the flap track fairings. With increasing spanwise position it moves forward towards the leading edge. On the inboard side of the two most outboard flap track fairings small flow separations are visible as well. In addition, the flow on the spanwise outer third of the wing lower surface is completely separated. On the nacelle lower surface a strong shock is visible at roughly 13% local chord followed by a small area of separated flow. Observing the pressure distributions on the upper surfaces of wing, pylon and nacelle in Fig. 3b no such phenomena can be observed. Due to the low angle of attack and high free stream Mach number only a weak shock is found on the wing located at around 80% local chord. No flow separations are visible on the upper surfaces from the simulation data.

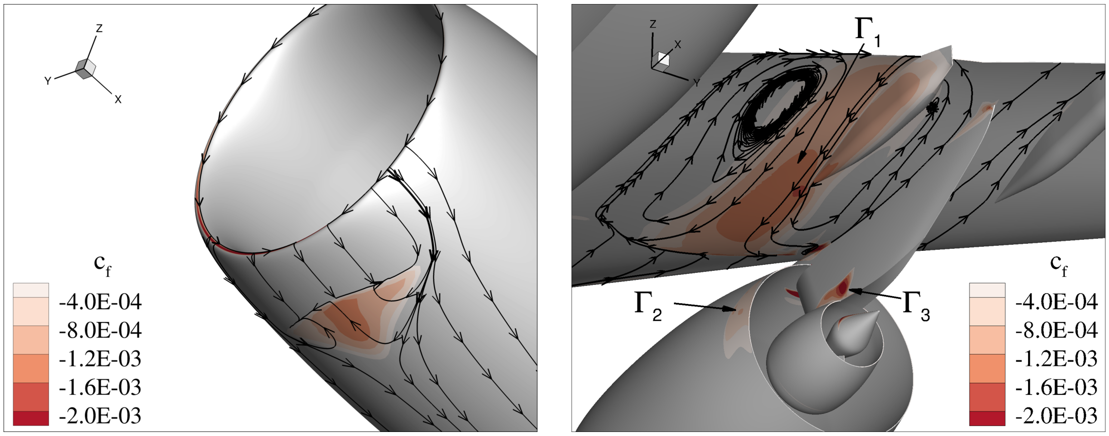

**(a) Nacelle lower side** **(b) Inboard wing**

**Fig. 4 Details of local flow separations on the wing lower surface at Re = 3.3 million, Ma = 0.84 and $\alpha = -4°$.**

Figure 4 provides a more detailed look at the individual phenomena. The shock-induced separation on the nacelle lower surface is shown in Fig. 4a. Contours of negative skin friction are shown in the region of interest. Note that a small portion of the inlet lip shows a region of negative $c_f$ as well. This, however, is related to the position of the inlet stagnation line which lies slightly inside the inlet. No separation on the leading edge of the nacelle inlet lip was observed. The actual shock-induced flow separation on the nacelle shows a region of reversed flow, represented by the skin friction lines plotted at and around the flow separation. The skin friction lines downstream of the separation are converging rapidly towards the center line of the nacelle lower surface. This indicates that the surrounding flow is filling up the low pressure region and therefore limiting the chordwise extension of the separation.

As already indicated by Fig. 3a the flow separation present on the inboard wing lower surface extends over a much larger area. This is supported by the course of the wall shear stress represented by skin friction lines in Fig. 4b proving that the flow separation extends up to the trailing edge of the wing and that it involves a large area of recirculation ($\Gamma_1$). Further inspection of Fig. 4b reveals additional small areas of negative $c_f$. One is located on the inboard side of the outer nacelle surface towards the trailing edge ($\Gamma_2$). Further analysis suggests that this is also a shock-induced separation, the shock on the nacelle at this location being a result of an interaction of the nacelle and wing pressure fields. Nevertheless, it was found that this shock-induced separation is very weak compared to the previously discussed flow interactions (see also corresponding $c_f$-magnitude in Fig. 4b). Another indication of separated flow is found at the intersection of pylon and core towards the trailing edge of the core body ($\Gamma_3$). Although not shown here, this region of negative skin friction coefficient is also present on the opposite side of the pylon. It results from the interaction of a shock in the bypass nozzle with the corner flow and is additionally exacerbated by the pressure rise downstream. The latter is caused by expansion of the local cross section due to the declining core radius towards the trailing edge.

In the junction formed by the nacelle rear part, the inboard surface of the pylon, and the wing lower surface, a corner flow separation can be observed in Fig. 4b. A more detailed representation of this phenomenon is given in Fig. 5 providing a close up view on the inboard nacelle-pylon-wing junction as viewed from the rear below. The surface pressure distribution in Fig. 5a shows parts of the shock on the wing that was associated with UHBR induced buffet on the wing lower surface. In the junction, the shock is smeared out due to the corner flow separation visible in Fig. 5b. As a result, no sudden pressure rise occurs and the pressure recovery happens more smoothly. At the current time it is not known if this corner stall is related to or affected by the large flow separation on the wing lower surface.

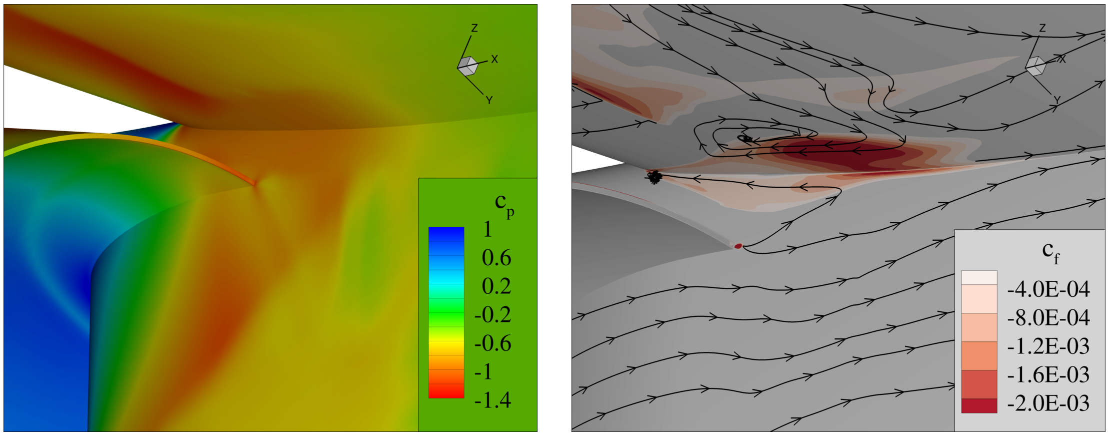

**(a) Surface pressure distribution** **(b) Local flow separation**

**Fig. 5 Details of resulting channel flow in the wing-pylon-nacelle junction at Re = 3.3 million, Ma = 0.84 and $\alpha = -4°$.**

The described effects provide a variety of shock-induced separation phenomena on a complex transport aircraft geometry. Their mutual dependency and interaction is yet to be understood. With the WMLES simulations provided in Secs. IV.B and IV.C a first step to gain further insight into these phenomena is undertaken.

### B. Turbulence resolving simulations of flow phenomena at the lower side of the nacelle

This section focuses on the shock boundary-layer interaction located at the nacelle lower side (Fig. 4a) and provides comparisons between RANS, turbulence resolving simulations as well as experimental results obtained for $Ma = 0.84$ and $\alpha = -4°$. Note, however, that the nacelle is still coupled to the XRF1 aircraft configuration. In the following, results of the embedded SST-WMLES methodology with synthetic turbulence injection, as described in Sec. III.D, are presented and compared to a SST-RANS solution. The SST-RANS solution, which was analysed in the previous Sec. IV.A, is used as initial condition for the scale resolving simulation. A normalized physical time step width of $\Delta t^+ = 0.4 = \mu \Delta t {Re_\tau}^2/(\delta^2 \rho)$ is selected which corresponds to $\Delta t = 5.5 \cdot 10^{-8}$ s and is in accordance with relevant literature [30, 45]. The employed time step size equals to $1/16750$ convective time units (CTU). A CTU is defined as $\mathrm{CTU} = c/\overline{U_{\mathrm{inf}}}$, where $c$ represents the nacelle chord length. This choice results into convective CFL numbers fulfilling $\mathrm{CFL} \leq 1$ in the entire LES region. The total simulation time amounts to 5.0 CTU.

### *1. Transient simulation phase*

Within an initial transient simulation phase the injected turbulence develops through the entire refinement region up to the nacelle trailing edge. Furthermore, the modelled turbulence of the initial SST RANS solution is dissipated and convected out of the WMLES region (cf. Fig. 2b and Fig. 14 for an overview of the refinement region for WMLES). To give an impression of the temporal development of the flow at the lower side of the nacelle, Fig. 6 depicts three snapshot results over time of Mach number slices through the transonic flow region. While the upper image shows the SST-RANS start solution for the SST-WMLES, the middle and lower image show results of the turbulence resolving simulation method with pronounced turbulent structures. It is apparent that after the switch from modelled to resolved turbulence the transonic shock front is moving downstream (cf. upper and middle image of Fig. 6). However, only minor qualitative differences can be observed between the second ($t = 1.6$ CTU) and the third snapshot ($t = 3.1$ CTU), indicating a convergence of the unsteady simulation. A more quantitative analysis of the convergence is given in Fig. 12a and Fig. 12b in Sec. IV.B.3 revealing a convergence after 2 CTU. For a more detailed description of this initial time period the reader is referred to [41]. For the subsequently presented analysis, averaged flow quantities are computed from $2 \leq t/\mathrm{CTU} \leq 5$ CTU excluding the transient phase of the simulation.

### *2. Analysis of temporal averaged flow quantities*

Fig. 7a shows the average skin friction distribution of the WMLES solution. The WMLES region is located in the interval $0.08 \leq x/c \leq 1$ and $0.08 \leq y/c \leq 0.59$. Significant differences within the refinement region compared to the SST RANS solution (Fig. 7b) appear. First of all, the area of recirculation ($c_f \leq 0$, indicated by black line) is reduced significantly. Furthermore, the shock front is shifted from its minimum position $x/c = 0.13$ downstream to an average position of $x/c = 0.17$. It should be noted that the C-shaped shock front in the RANS simulation is straightened and partially formed into a line parallel to the y-axis when applying the WMLES. In addition, smaller values of $c_f$ as well as regions with flow separation are present at the lateral boundaries of the WMLES region ($y/c = 0.1$, $y/c = 0.6$). This is due to locally underresolved turbulence and is caused, among other things, at the lateral edges of the synthetic turbulence injection region. Here, the STG is not directly attached to the lateral RANS regions but small gaps without STG treatment are present in the WMLES region. A more detailed discussion of this local flow behaviour can be found in [41] for the same flow configuration. With regard to the colour change of the contour variable $\overline{c_f}$ at the location of the shock front, a rapid change from yellow (high values) to blue (low values) is visible. This change can also be observed in Fig. 8a which shows $\overline{c_f}$ profiles at $\varphi = 180\,^\circ$. The rapid changes indicate that no distinct shock movement

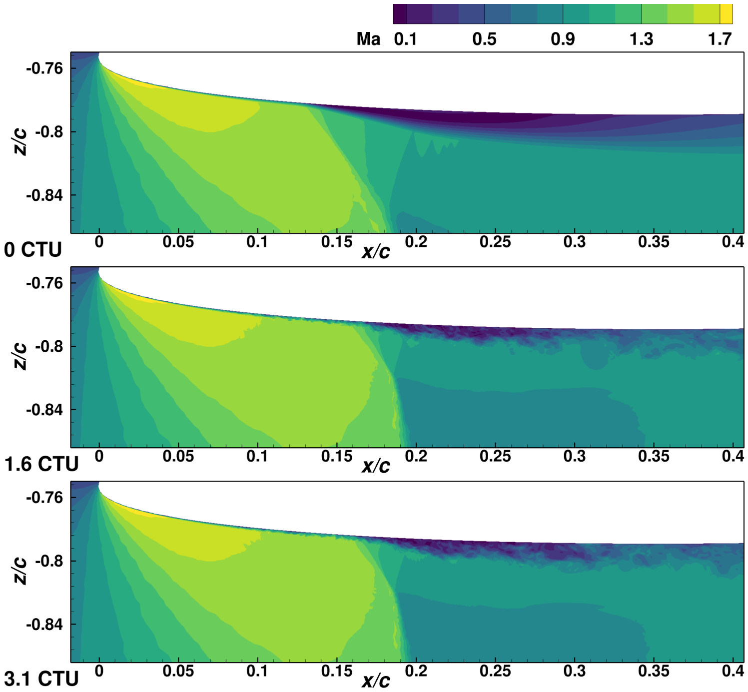

**Fig. 6 Ma-number fields of a slice through the refinement volume ($y/c = 0.24$) for the SST-RANS start solution (0 CTU) and snapshot solutions of the subsequent SST-WMLES for two different time steps (Re = 3.3 million, Ma = 0.84 and $\alpha = -4\,°$).**

is present for $t \geq 2\,$CTU. Otherwise a smoothed $c_f$-distribution would occur. A further look to Fig. 8a shows that the $x/c$-range, where $c_f \leq 0$, is of much smaller extent. Additionally, the magnitude of $c_f$ is reduced compared to the RANS simulation in this area.

A quantitative analysis of pressure distributions in $x$-direction is provided by Fig. 9a. In this diagram pressure profiles of RANS, SST-WMLES and experimental data for $\varphi = 180\,°$ are shown. The experimental values originate from local pressure sensors and were obtained from wind tunnel tests in ETW (cf. [1]). Comparing RANS and SST-WMLES results, good agreement upstream of the shock ($x_s/c \leq 0.13$) is observed. Both curves show almost identical results for $x/c \geq 0.35$ which is related to the area downstream of the shock boundary-layer interaction. As already described for Fig. 7b and Fig. 8a relevant deviations occur with regard to the shock front location. This is shifted downstream from $x_s/c = 0.13$ (RANS) to $x_s/c = 0.16$ (SST-WMLES). The numerical pressure profiles are validated by experimental data which demonstrate good agreements for both simulation approaches. With regard to the shock front position $x_s$ the pressure sensors indicate its location within the interval $0.13 \leq x_s/c \leq 0.23$.

Fig. 9 contains the time averaged $x$-velocity distributions of experimental PIV and numerical SST-WMLES field data of the transonic flow region below the nacelle and resolve the spatial extension of the shock in $z$-direction. For more information about the employed PIV test environment provided by DLR, the reader is referred to [27]. Note that the $y$-coordinate of the diagrams is not constant but the lower end of the volume slice is slightly tilted towards the

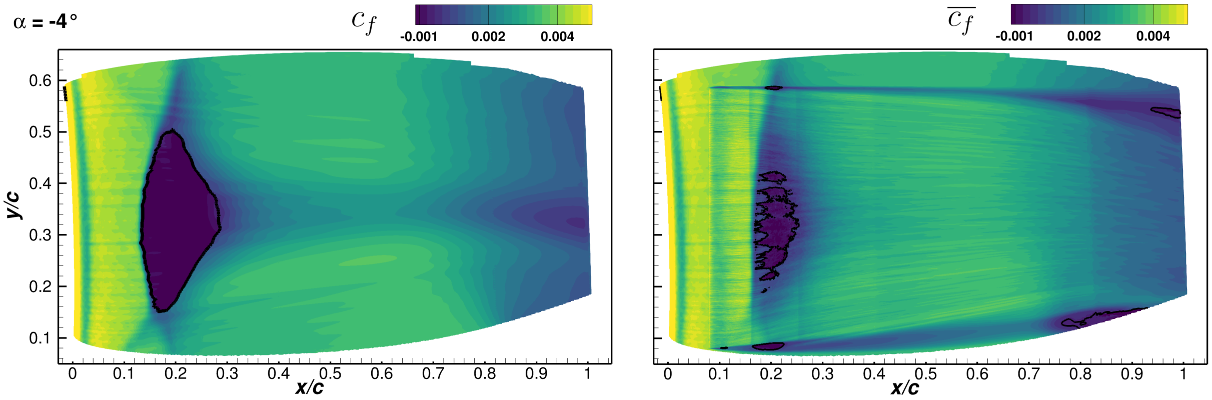

(a) SST-RANS

(b) SST-WMLES

**Fig. 7 Average skin friction distributions ($c_f$) of a SST-RANS solution (left) and a WMLES simulation (right) of the lower nacelle surface at Re = 3.3 million, Ma = 0.84 and $\alpha = -4°$.**

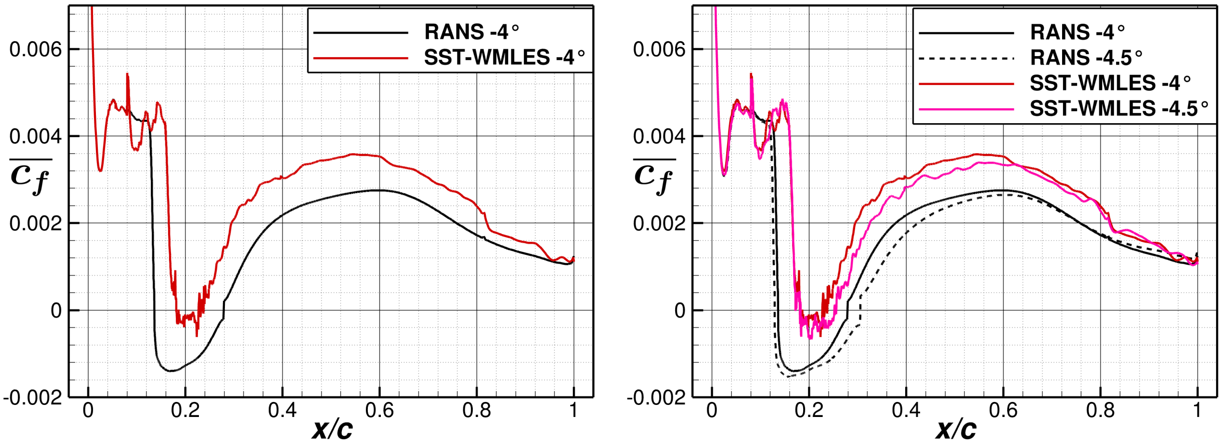

(a)

(b)

**Fig. 8 Mean skin friction profiles $\overline{c_f}$ of RANS and SST-WMLES at the nacelle nacelle lower surface at $\varphi = 180°$ for different angles of attack $\alpha$ at Re = 3.3 million and Ma = 0.84.**

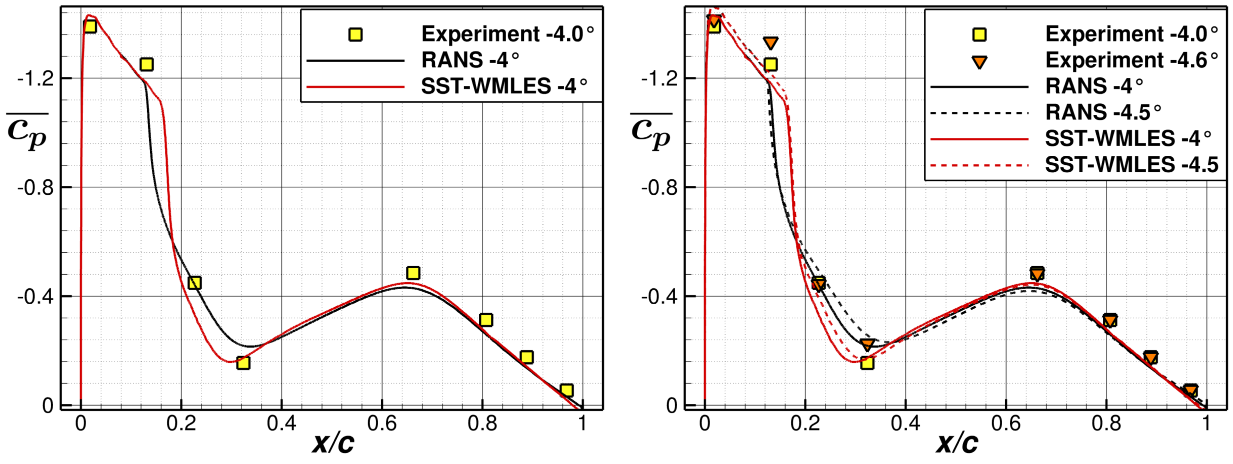

**(a)** **(b)**

**Fig. 9 Pressure profiles of numerical and experimental data at the nacelle nacelle lower surface at $\varphi$ = 180° for different angles of attack $\alpha$ at Re = 3.3 million and Ma = 0.84.**

fuselage. The volume plane is defined by the points $P_i(x/c \mid y/c \mid z/c)$ with $P_1(0|1.557|-0.8)$, $P_2(0|1.481|-1.1)$ and $P_3(0.4|1.488|-1.1)$, where $c$ is defined as the chord length of the nacelle. In the context of the presented field data $x/c$ represents the x-distance to the most upstream position of the nacelle, $y/c$ the y-distance to the symmetry plane of the half model and $z/c$ the negative z-distance to the tip of the aircraft nose. Both distributions are nondimensionalized with their respective time averaged farfield velocity $\overline{U_{\text{inf}}}$. In the SST-WMLES data in Figure 10a, a region with significantly enhanced velocity, which corresponds to a supersonic flow region, is clearly visible and evolves directly downstream of the nacelle leading edge. The $x$-velocity distribution has its highest values with $\overline{u_x}/\overline{U_{\text{inf}}} \geq 1.6$ in the upstream area of the nacelle nearby the wall and decreases in negative $z/c$ direction. The supersonic region is terminated with a distinct shock front at $x/c \approx 0.2$. In the near-wall region, however, the shock shows a typical forward displacement and finally ends at $x/c \approx 0.16$ at the nacelle lower surface. This is in agreement with the numerical $\overline{c_f}$ and pressure data in Fig. 7b and Fig. 9a. Additionally, the AOR is also visible in the volume slice but limited to a rather narrow near-wall region. The corresponding experimental PIV data of the same volume slice are shown in Fig. 10b. Note, however, that a different Reynolds number of $Re = 6.6 \times 10^6$ is present which limits a direct comparison of both volume slices ($Re = 3.3 \times 10^6$ in SST-WMLES). Furthermore, due to an insufficient number of PIV seeding particles in the near-wall region, the corresponding field data is not reliable and was therefore excluded. The topology of the supersonic flow region shows similarities to the WMLES data (cf. course of solid isolines with $\overline{u_x}/\overline{U_{\text{inf}}} = 1.2$). However, the shock area with higher $x$-velocity (e.g. $\overline{u_x}/\overline{U_{\text{inf}}} \geq 1.4$) is visibly smaller in the PIV data (cf. course of dashed isolines) and indicates a weakening of the supersonic flow region. Furthermore, the average shock location of the PIV data is slightly shifted downstream ($x_s/c \approx 0.22$). Both, the backward shift and the weakened supersonic region can potentially

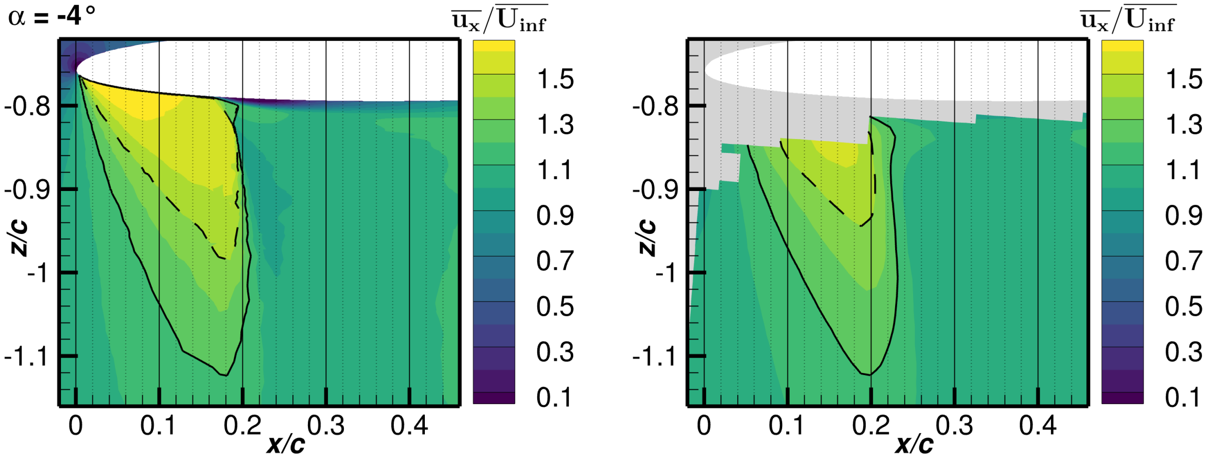

**(a) SST-WMLES,** $Re = 3.3 \times 10^6$ **(b) PIV,** $Re = 6.6 \times 10^6$

**Fig. 10 Normalised $\overline{u_x}$-velocity field data for SST-WMLES and experimental PIV results below the nacelle at Ma = 0.84 and $\alpha = -4°$.**

be attributed to a Reynolds number effect. As published in [46], transonic wind tunnel results of an NACA airfoil demonstrate that increasing Reynolds numbers lead to a weakening of shock boundary-layer interaction and a rearward movement of the shock front location. Another noticeable feature of the PIV data is the significantly more smeared shock area. However, this can partly be attributed to statistically non-converged PIV data (i.e. the running average of the spatially averaged $\overline{u_x}$-velocity field exhibits a slight trend over time) and is probably not due to a shock movement.

### *3. Flow field dynamics*

In order to provide insights into the dynamics of the SST-WMLES simulation, the standard deviation of the surface pressure coefficient $\sigma(c_p)$ is calculated and represented in Figure 11a. A flow region with pronounced $c_p$ dynamics is present at the shock front location within the refinement area (cf. Fig. 7b to inspect the location of the shock front). The width of this fluctuation band amounts to approximately $0.02\,c$ and can probably be attributed to small shock oscillations in $x-$direction. Additionally, a region with distinct $c_p$ dynamics occurs directly downstream of the AOR around $x/c = 0.25$ (the location of the AOR is highlighted in Fig. 7b), which can be attributed to the impingement of turbulent structures on the nacelle surface in the area of reattachment of the boundary layer. It is important to mention that the standard deviations of the URANS regions surrounding the WMLES focus area in lateral direction are close to zero. Thus, albeit the shock front being located in these URANS regions (cf. Fig. 7b) no dynamics are observed. For shock buffet however, a shock movement is expected to also affect the surrounding URANS region for this choice of the refinement area. Furthermore, there are additional regions with higher $\sigma(c_p)$ values, which are, however, not directly related to the shock boundary-layer interaction: initially, at the position of the STG ($x/c = 0.08$), which is due to the injection of turbulent fluctuations close to the wall. Moreover, the areas on the right hand side outside of the refinement

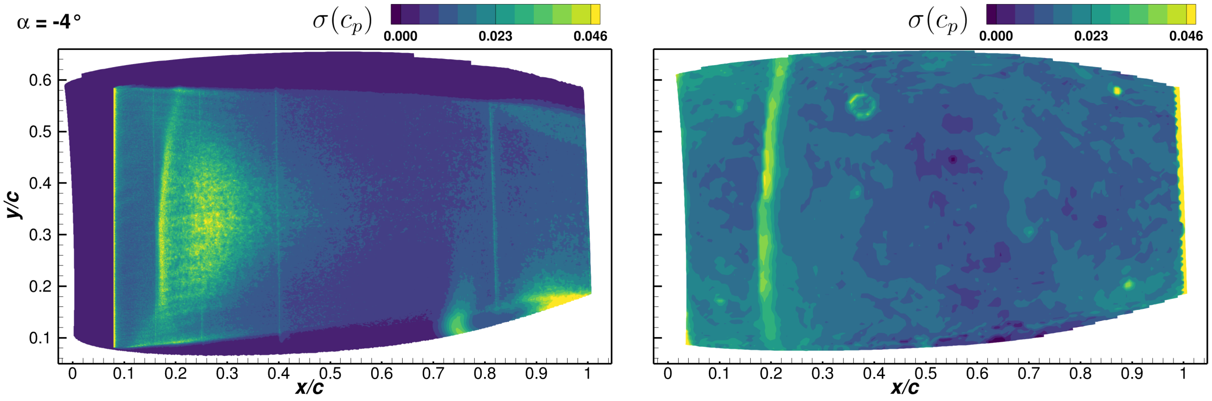

**(a) SST-WMLES**

**(b) unsteady PSP**

**Fig. 11 Analysis of the standard deviation of the pressure coefficient $\sigma(c_p)$ at the lower nacelle surface for numerical and experimental data at Re = 3.3 million, Ma = 0.84 and $\alpha = -4°$.**

region ($x/c = 0.75$, $y/c = 0.1$). These can be traced back to the earlier mentioned lateral gaps at $x/c = 0.08$ (cf. also [41]) with missing synthetic turbulence injection. This leads to regions with underresolved turbulence and small areas of recirculation with unsteady flow behaviour.

Figure 11b shows a $\sigma(c_p)$ distribution derived from unsteady PSP measurements. Details on this experimental method can be obtained from [1, 23–25]. Essentially, a curved stripe with increased $\sigma(c_p)$ values is visible with an otherwise approximately uniform, low $\sigma(c_p)$ distribution. In addition, there are minor, bright spots, which are, however, measurement artifacts which can probably be attributed to surface deviations or light reflections. With regard to the pressure sensor data in Fig. 9a, which shows a shock position in the interval $0.13 \leq x_s/c \leq 0.23$, it can be concluded that the location of the curved stripe in fact corresponds to the shock front position. Comparing the locations of the curved stripes of the WMLES and unsteady PSP data at a central lateral position $y/c = 0.32$, one obtains almost identical positions ($x_s/c = 0.17$ for WMLES and $x_s/c = 0.18$ for unsteady PSP). Additionally, the curvature, the thickness as well as the $\sigma(c_p)$ level of both stripes are very similar. However, in contrast to the WMLES data, there is no area with enhanced $\sigma(c_p)$ values downstream of the shock in the unsteady PSP data. A potential explanation could be that the shock does not induce flow separation with a corresponding AOR and thus no impinge of turbulent structures occurs in the area or reattachment. This explanation, however, can unfortunately not be validated by neither the velocity distribution of the PIV results in Fig. 10b (which does not provide data in vicinity of the wall) nor the experimental pressure data in Fig. 9a (which does not resolve the corresponding area of the flow).

To address the dynamics of the entire refinement area, pressure and skin friction coefficients were spatially averaged within the WMLES region. Temporal developments of these quantities ($\langle c_f \rangle$ and $\langle c_p \rangle$) are shown in Fig. 12a and 12b (solid red curves). After an initial variation of $\langle c_f \rangle$, which is due to transient processes, it remains constant for $t \geq 1.5$ CTU. A similar trend is present for $\langle c_p \rangle$, showing significantly reduced fluctuations for $t \geq 2$ CTU. These results

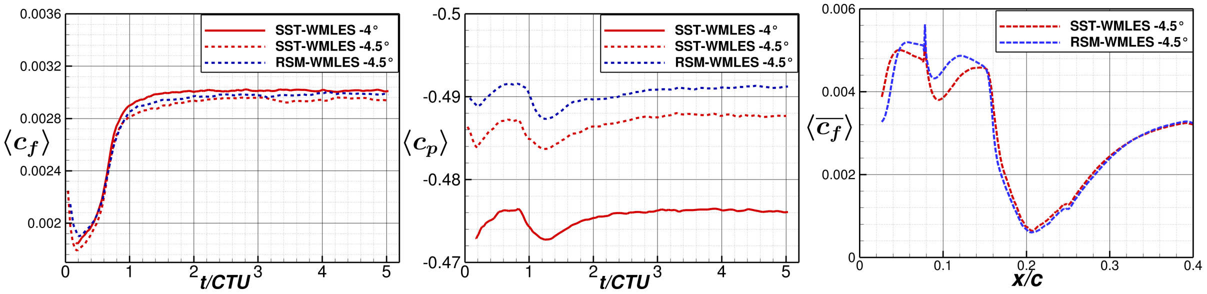

**(a)** **(b)** **(c)**

**Fig. 12 (a), (b): Temporal evolution of spatially averaged flow quantities. The spatial averaging involves surface data of the entire WMLES region. (c): Circumferential average of the WMLES area of time averaged $\overline{c_f}$ distribution.**

also justify the applied averaging protocol which starts at 2 CTU. Furthermore, it can be concluded that due to the small fluctuations of integral quantities of the refinement area (which covers 32 % of the outer nacelle chasing) a negligible impact on the entire aircraft configuration is expected.

## C. Turbulence resolving simulations for a steeper angle of attack

In the previous section only minor dynamics of the transonic shock front have been observed in the presented numerical and experimental results at the lower side of the nacelle. As mentioned in Sec. IV.A, we observe that the angle of attack is the key driver for shock-induced separation in RANS simulations for this flow configuration. Thus, steepening the angle of attack to values below $-4\,^\circ$ might potentially enhance shock front dynamics. Because of this, numerical and experimental investigations of the nacelle lower side for an even lower angle of attack of $\alpha = -4.5\,^\circ$ are performed and presented in the following. As in the entire paper, the nacelle is still coupled to the XRF1 aircraft configuration. The total simulation time amounts again to 5 CTU and time averages of selected flow quantities were calculated for $t \geq 2$ CTU.

### *1. Differences in RANS solutions*

As a first step of the analysis the two SST-RANS solutions with $\alpha = -4\,^\circ$ and $\alpha = -4.5\,^\circ$ are compared. The main effect for the larger negative angle of attack is the slightly enhanced shock boundary-layer interaction. This is indicated by a longer AOR (in streamwise direction $x$) as it can be seen in the skin friction distributions of Fig. 7a and 13a as well as by the $c_f$ profiles (cf. solid and dashed black curves in Fig. 8b). Additionally, the negative $c_f$-level in this region is further reduced for $\alpha = -4.5\,^\circ$ which represents an higher intensity of the AOR. Besides these differences the surrounding area of the AOR is less affected. For example, the $\varphi = 180\,^\circ$ shock position is shifted by less than 0.01 $c$ in upstream direction (cf. solid and dashed black curves in Fig. 8a and 9a).

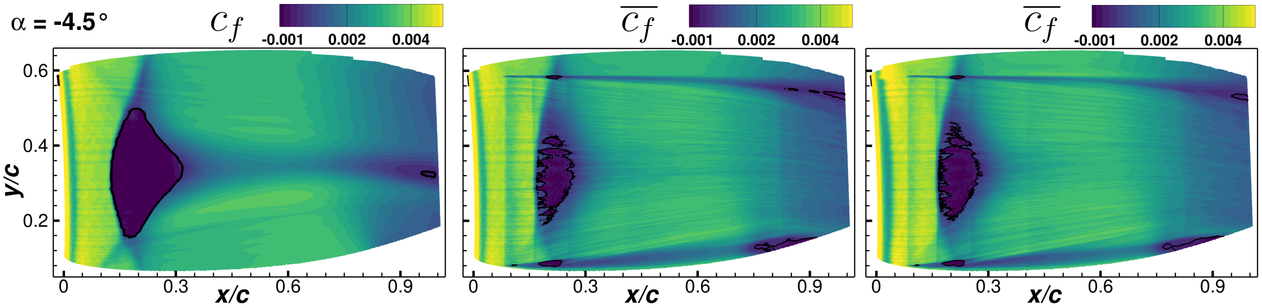

**(a) SST-RANS** **(b) SST-WMLES** **(c) RSM-WMLES**

**Fig. 13 Time-averaged skin friction distributions ($\overline{c_f}$) of the lower nacelle surface for different numerical approaches at Re = 3.3 million, Ma = 0.84 and $\alpha = -4.5\,°$.**

### *2. Comparison of SST-WMLES solutions*

The SST-WMLES results for different angles of attack show similar trends as the RANS solutions. The enhanced shock boundary-layer interaction is visible in form of an enlarged AOR (cf. Fig. 7b and Fig. 13b). Note that the lateral extension of the AOR remains almost constant and is only enlarged in streamwise direction. Again, the negative $c_f$-level is further reduced for the steeper angle of attack (cf. red and pink lines in Fig. 8a). Furthermore, the average 180 ° shock positions show no effect of the decrease of $\alpha$ and remains at $x_s/c = 0.17$. To assess the dynamics of the WMLES simulation, various perspectives on the data are evaluated. Initially, the gradients at the shock front position in $c_p$ and $c_f$ line plots (cf. Fig. 8b and 9b): identical and steep gradients for both angle of attacks indicate no significant change in the dynamics around the shock fronts. Furthermore, the standard deviation of the pressure coefficient surface distribution in Fig. 15a shows a comparable distribution as for $\alpha = -4\,°$ (cf. Fig. 11a). Minor differences only occur in the area of reattachment with slightly increased standard deviations of $c_p$ for $\alpha = -4.5\,°$. This increase is potentially caused by the larger AOR enhancing the impingement of turbulent structures on the nacelle surface. An additional comparison of the dynamics in the WMLES simulations is provided in Fig. 12a and 12b. As before, after the transient time of 2 CTU the fluctuation of the spatially and temporally averaged $\langle\overline{c_p}\rangle$ and $\langle\overline{c_f}\rangle$) distributions (spatial averaging is applied over the entire refinement region) are significantly reduced. Thus, no relevant integral dynamics due to shock boundary-layer interaction are present for both angles of attacks.

### *3. RSM-WMLES results for $\alpha = -4.5\,°$*

For the larger negative angle of attack, a further scale-resolving simulation was carried out using a newly developed RSM-WMLES method (cf. Sec. III.D). A snapshot result at $t = 5.0\,$CTU of this simulation is provided in Fig. 14 and gives an impression of the turbulent structures on the lower surface of the nacelle. The different magnitudes of the turbulent length scale, which increase in streamwise direction, are particularly noteworthy. In addition, hairpin vortices are visible over a large area of the refinement region. Compared to the $\overline{c_f}$ distribution of the corresponding

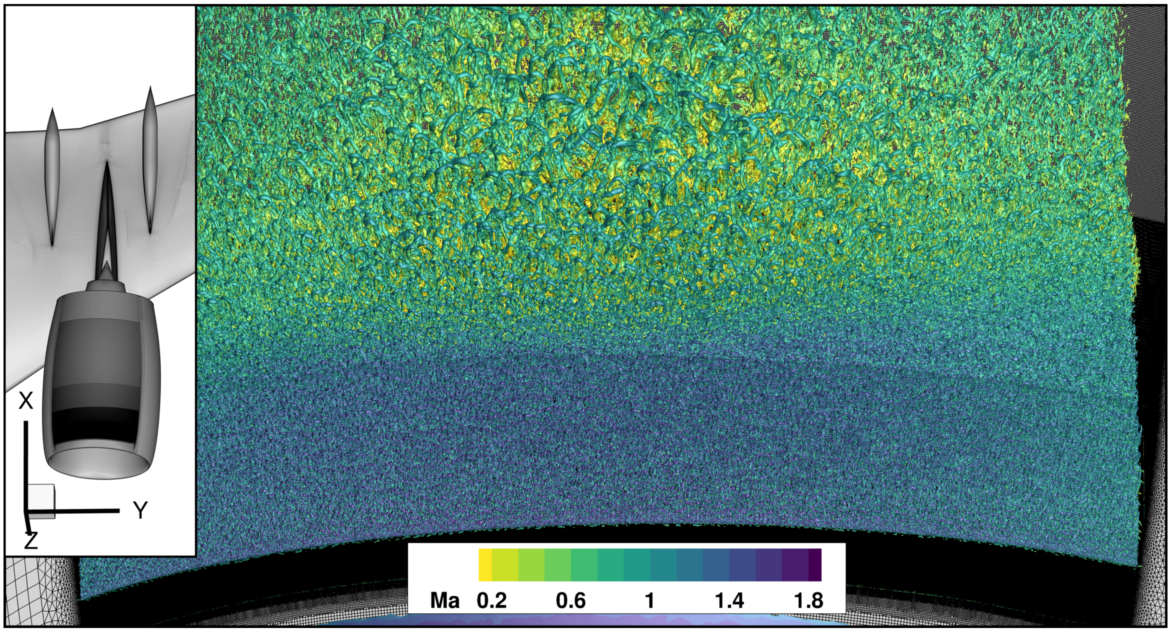

**Fig. 14 Isosurface of Q-criterion $Q = 10^{10}/\mathrm{s}^2$ at nacelle lower surface for RSM-WMLES at $t = 5.0\,\mathrm{CTU}$ (Re = 3.3 million, Ma = 0.84 and $\alpha = -4.5\,°$).**

SST-WMLES, very good agreement can be seen for the most part (cf. Fig. 13b, 13c). There are only minor differences in the AOR, which is slightly more pronounced for the RSM-WMLES. More significant differences occur directly downstream of the position of the STG at the RANS-LES interface ($x_{\mathrm{STG}}/c = 0.08$) (Fig. 13c). The decay in $\overline{c_f}$ is less pronounced and the original $\overline{c_f}$ level (directly upstream of the STG) is reached earlier. This behaviour is shown again in Fig. 12c, where the $\overline{c_f}$ surface distribution is averaged in circumferential direction within the LES zone. It is clearly visible that the $\langle\overline{c_f}\rangle$ dip downstream of the STG is reduced and also shortened. Thus, it is shown that the RSM-WMLES has an attenuating effect on the so-called grey area induced by the RANS-LES interface. This can potentially be explained by the more sophisticated injection of synthetic turbulence in the RSM-WMLES. Here, the STG obtains six independent modelled Reynolds stresses (with realistic anisotropy in the normal stresses) from the upstream RANS solution as input and translates them into resolved velocity fluctuations (cf. Ref. [43]).

However, these upstream differences do not have strong downstream effects on the flow, so that a similar flow behaviour occurs again in both simulations downstream of the shock locations (cf. Fig. 12c). Furthermore, there are no pronounced differences in the standard deviations of the pressure coefficient fields (Fig. 15b) as well as the time series plots in Fig. 12a and 12b. Consequently, there is no significant shock dynamics present for the RSM-WMLES either. These results are plausible insofar as the RANS models responsible for the wall modelling (SSG/LRR RSM and Menter's SST) have structural similarities and only minor differences should arise for flows over flat surfaces. For intersection regions of aircraft components with corner flows, however, a higher accuracy is to be expected for the RSM-WMLES model and thus potentially more significant deviations from the SST-WMLES.

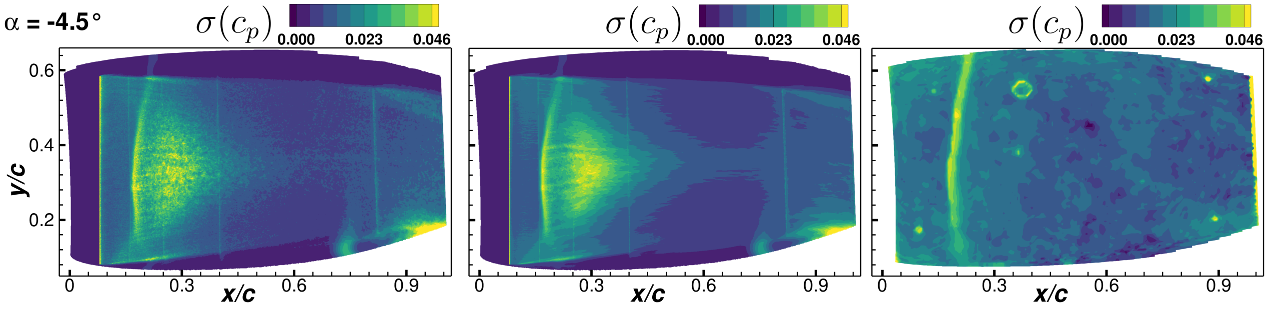

**(a) SST-WMLES** **(b) RSM-WMLES** **(c) unsteady PSP**

**Fig. 15 Comparison of the standard deviation of the pressure coefficient $\sigma(c_p)$ of numerical ((a), (b)) and experimental data (c) at Re = 3.3 million, Ma = 0.84 and $\alpha = -4.5°$.**

*4. Effect on experimental data and comparison to simulation results*

Comparing the unsteady PSP data for $\alpha = -4.5°$ in Fig. 15c with the results of $\alpha = -4°$ in Fig. 11b, shows that both distributions are very similar and especially the location, intensity and thickness of the intensity band is hardly changed. Again, the shock front locations of both numerical and experimental results still coincide. For example, the $\sigma(c_p)$ peak of SST-WMLES and RSM-WMLES at $\varphi = 180°$ is located at $0.175\,x/c$. The corresponding location of the unsteady PSP data, can be found at $0.185\,x/c$. Thus, steepening the angle of attack to $-4.5°$ has no significant impact on the shock front dynamics which is also in agreement with the WMLES results.

## V. Conclusions

Numerical and experimental investigations of the XRF1 transport aircraft configuration with UHBR nacelles at transonic off-design flow conditions were performed. Statistical SST-RANS simulations provided an overview of aerodynamic phenomena occurring on the configuration at high-speed off-design conditions as well as deeper insights into complex, three dimensional phenomena associated with the UHBR integration. Several areas of shock-induced boundary layer separation were identified and could be traced back to the close coupling of the nacelle to the lower wing. These examinations served as a starting point for further examinations with scale resolving WMLES approaches (SST-WMLES, RSM-WMLES) of a local shock boundary-layer interaction at the lower surface of the nacelle.

A main difference between RANS and WMLES solutions of the transonic shock is a weaker shock boundary-layer interaction for WMLES. This was visible in a significantly reduced AOR and a weaker backflow. Furthermore, a significant shift of the shock position of $0.04\,x/c$ in downstream direction was observed. The time averaged shock position as well as shock curvature on the nacelle surface, obtained by WMLES, were found to be in very good agreement with experimental data resulting from unsteady PSP measurements and time resolved PIV. A further research objective was a sensitivity study on angle of attack variation. By lowering the angle of attack from $\alpha = -4°$ to $\alpha = -4.5°$ enhanced shock boundary-layer interaction is observed in RANS and both WMLES results. The larger negative angle of attack leads to an extension of the area of recirculation in streamwise direction and slightly pronounced backflow in both numerical approaches. However, the average shock position in the WMLES was not affected, which is also in agreement with the employed experimental methods. It is important to mention that the newly developed RSM-WMLES method shows consistent results compared to the established SST-WMLES as well as to unsteady PSP results. Thus, the RSM-WMLES is successfully validated for a transonic flow including flow separation. With regard to the shock front dynamics no relevant shock movements for the WMLES simulations were observed for both angles of attack. Neither the standard deviations of the $c_p$ distributions nor the time series of integral $c_p$ and $c_f$ values related to this flow area show significant fluctuations that can be attributed to shock buffet. Thus, no buffet phenomenon is present for the chosen flow conditions at the lower nacelle surface which is also in accordance with unsteady PSP data.

The very good agreements of WMLES and unsteady PSP data with regard to average shock positions, shock curvatures and shock dynamics demonstrate a high reliability of SST-WMLES and RSM-WMLES in this context. Such good agreements have also been observed in [9], where the semi-open channel, bounded by pylon, lower wing and fuselage, of the same model configuration was investigated with the RSM-WMLES method. Thus, the higher computational as well as higher research effort pays back using these more sophisticated approaches. In future research on this configuration, higher Reynolds numbers will be addressed, which will also enable a direct comparison to existing PIV measurement data. Furthermore, a realistic engine jet will be included in the numerical setup to evaluate its effects on the transonic flow with regard to shock buffet.

## Acknowledgments

The authors gratefully acknowledge the Deutsche Forschungsgemeinschaft DFG (German Research Foundation) for funding this work in the framework of the research unit FOR 2895. The authors would like to thank the Helmholtz Gemeinschaft HGF (Helmholtz Association), Deutsches Zentrum für Luft- und Raumfahrt DLR (German Aerospace Center) and Airbus for providing the wind tunnel model and financing the wind tunnel measurements as well as public support to mature the test methods applied by DLR and ETW. Additionally, the authors gratefully acknowledge the computing time granted by the Resource Allocation Board and provided on the supercomputer Lise and Emmy at NHR@ZIB and NHR@Göttingen as part of the NHR infrastructure. Parts of the calculations for this research were conducted with computing resources under the project nii00164. Furthermore, the authors gratefully acknowledge the scientific support and HPC resources provided by DLR. The HPC system CARO is partially funded by "Ministry of Science and Culture of Lower Saxony" and "Federal Ministry for Economic Affairs and Climate Action".

## References

[1] Lutz, T., Kleinert, J., Waldmann, A., Koop, L., Yorita, D., Dietz, G., and Schulz, M., "Research initiative for numerical and experimental studies on high-speed stall of civil aircraft," *Journal of Aircraft*, Vol. 60, No. 3, 2023, p. 623–636.

https://doi.org/10.2514/1.c036829.

[2] Berry, D. L., "The boeing 777 engine/airframe integration aerodynamic design process," *ICAS PROCEEDINGS*, Vol. 19, AMERICAN INST OF AERONAUTICS AND ASTRONAUTICS, 1994, pp. 1305–1305.

[3] Rudnik, R., Rossow, C.-C., and Frhr. v. Geyr, H., "Numerical simulation of engine/airframe integration for high-bypass engines," *Aerospace Science and Technology*, Vol. 6, No. 1, 2002, p. 31–42. https://doi.org/10.1016/s1270-9638(01)01139-7.

[4] Magrini, A., Benini, E., Yao, H.-D., Postma, J., and Sheaf, C., "A review of installation effects of ultra-high bypass ratio engines," *Progress in Aerospace Sciences*, Vol. 119, 2020, p. 100680. https://doi.org/10.1016/j.paerosci.2020.100680.

[5] Soda, A., and Tefy, T., *Numerical investigation of wing-nacelle interference effects at transonic flow conditions for a generic transport aircraft configuration*, Springer Berlin Heidelberg, 2004, p. 82–90. https://doi.org/10.1007/978-3-540-39604-8_11.

[6] Dietz, G., Mai, H., Schröder, A., Klein, C., Moreaux, N., and Leconte, P., "Unsteady wing-pylon-nacelle interference in transonic flow," *Journal of Aircraft*, Vol. 45, No. 3, 2008, p. 934–944. https://doi.org/10.2514/1.31363.

[7] Browne, O. M., Maldonado, D., Housman, J. A., Duensing, J., and Milholen, W. E., "Simulating transonic buffet aerodynamics for the boeing transonic truss-braced wing aircraft," *AIAA SCITECH 2024 Forum*, American Institute of Aeronautics and Astronautics, 2024. https://doi.org/10.2514/6.2024-0065.

[8] Spinner, S., and Rudnik, R., "Experimental assessment of wing lower surface buffet effects induced by the installation of a UHBR nacelle," *CEAS Aeronautical Journal*, Vol. 15, No. 1, 2022, p. 49–59. https://doi.org/10.1007/s13272-022-00632-z.

[9] Spinner, S., Rudnik, R., Herr, M., Probst, A., and Radespiel, R., "Scale resolving simulation of buffet effects induced by ultrahigh bypass ratio nacelle installation," *Journal of Aircraft*, Vol. 62, No. 3, 2025, p. 551–563. https://doi.org/10.2514/1.c038119.

[10] Dandois, J., "Experimental study of transonic buffet phenomenon on a 3D swept wing," *Physics of Fluids*, Vol. 28, No. 1, 2016. https://doi.org/10.1063/1.4937426.

[11] Sugioka, Y., Koike, S., Nakakita, K., Numata, D., Nonomura, T., and Asai, K., "Experimental analysis of transonic buffet on a 3D swept wing using fast-response pressure-sensitive paint," *Experiments in Fluids*, Vol. 59, No. 6, 2018. https://doi.org/10.1007/s00348-018-2565-5.

[12] Paladini, E., Dandois, J., Sipp, D., and Robinet, J.-C., "Analysis and comparison of transonic buffet phenomenon over several three-dimensional wings," *AIAA Journal*, Vol. 57, No. 1, 2019, p. 379–396. https://doi.org/10.2514/1.j056473.

[13] Koike, S., Ueno, M., Nakakita, K., and Hashimoto, A., "Unsteady pressure measurement of transonic buffet on NASA common research model," *34th AIAA Applied Aerodynamics Conference*, American Institute of Aeronautics and Astronautics, 2016. https://doi.org/10.2514/6.2016-4044.

[14] Lutz, T., "Going for experimental and numerical unsteady wake analyses combined with wall interference assessment by using the NASA CRM-model in ETW," *51st AIAA Aerospace Sciences Meeting including the New Horizons Forum and Aerospace Exposition*, American Institute of Aeronautics and Astronautics, 2013. https://doi.org/10.2514/6.2013-871.

[15] Sartor, F., and Timme, S., “Delayed detached–eddy simulation of shock buffet on half wing–body configuration,” *AIAA Journal*, Vol. 55, No. 4, 2017, p. 1230–1240. https://doi.org/10.2514/1.j055186.

[16] Masini, L., Timme, S., and Peace, A. J., “Scale-resolving simulations of a civil aircraft wing transonic shock-buffet experiment,” *AIAA Journal*, Vol. 58, No. 10, 2020, p. 4322–4338. https://doi.org/10.2514/1.j059219.

[17] Ehrle, M., Waldmann, A., Lutz, T., and Krämer, E., “Simulation of transonic buffet with an automated zonal DES approach,” *CEAS Aeronautical Journal*, Vol. 11, No. 4, 2020, p. 1025–1036. https://doi.org/10.1007/s13272-020-00466-7.

[18] Ghate, A. S., Kenway, G. K., Stich, G.-D., Browne, O. M., Housman, J. A., and Kiris, C. C., “Transonic lift and drag predictions using wall-modelled large eddy simulations,” *AIAA Scitech 2021 Forum*, American Institute of Aeronautics and Astronautics, 2021. https://doi.org/10.2514/6.2021-1439.

[19] Tamaki, Y., and Kawai, S., “Wall-modeled LES of transonic buffet over NASA-CRM using Cartesian-grid-based flow solver FFVHC-ACE,” *AIAA SCITECH 2023 Forum*, American Institute of Aeronautics and Astronautics, 2023. https://doi.org/10.2514/6.2023-0429, URL http://dx.doi.org/10.2514/6.2023-0429.

[20] Goc, K. A., Agrawal, R., Bose, S. T., and Moin, P., “Studies of transonic aircraft flows and prediction of initial buffet using large-eddy simulation,” *Journal of Aircraft*, Vol. 62, No. 3, 2025, p. 530–550. https://doi.org/10.2514/1.c038129.

[21] Humphries, P., Gillan, M., and Raghunathan, S., “A study of isolated nacelle flows at subsonic and transonic speeds,” *36th AIAA Aerospace Sciences Meeting and Exhibit*, American Institute of Aeronautics and Astronautics, 1998. https://doi.org/10.2514/6.1998-946.

[22] Tejero, F., MacManus, D., Sanchez-Moreno, F., Schreiner, D., Hill, A., Sheaf, C., and Ramirez-Rubio, S., “Aerodynamics of high-bypass-ratio aeroengine nacelles: numerical and experimental investigation,” *Journal of Aircraft*, Vol. 62, No. 4, 2025, p. 1004–1017. https://doi.org/10.2514/1.c038164.

[23] Yorita, D., Klein, C., Henne, U., Ondrus, V., Beifuss, U., Hensch, A.-K., Longo, R., Guntermann, P., and Quest, J., “Successful application of cryogenic pressure sensitive paint technique at ETW,” *2018 AIAA Aerospace Sciences Meeting*, American Institute of Aeronautics and Astronautics, 2018. https://doi.org/10.2514/6.2018-1136.

[24] Klein, C., Yorita, D., Henne, U., Kleindienst, T., Koch, S., and Ondrus, V., “Unsteady pressure measurements by means of PSP in cryogenic conditions,” *AIAA Scitech 2020 Forum*, American Institute of Aeronautics and Astronautics, 2020. https://doi.org/10.2514/6.2020-0122.

[25] Yorita, D., Henne, U., and Klein, C., “Time-resolved pressure-sensitive paint measurements for cryogenic wind tunnel tests,” *CEAS Aeronautical Journal*, Vol. 15, No. 1, 2023, p. 37–47. https://doi.org/10.1007/s13272-022-00637-8.

[26] Waldmann, A., Ehrle, M. C., Kleinert, J., Yorita, D., and Lutz, T., “Mach and Reynolds number effects on transonic buffet on the XRF-1 transport aircraft wing at flight Reynolds number,” *Experiments in Fluids*, Vol. 64, No. 5, 2023. https://doi.org/10.1007/s00348-023-03642-7.

[27] Bosbach, J., Konrath, R., Geisler, R., Philipp, F., Agocs, J., Kühn, C., and Koop, L., “Capturing unsteady flow phenomena at high speed stall conditions by adaptation and application of cryogenic PIV,” *AIAA SCITECH 2024 Forum*, American Institute of Aeronautics and Astronautics, 2024. https://doi.org/10.2514/6.2024-2665.

[28] Spinner, S., and Rudnik, R., “Design of a UHBR through flow nacelle for high speed stall wind tunnel investigations,” *Deutscher Luft- und Raumfahrt Kongress*, 2021. https://doi.org/10.25967/550043.

[29] Eisfeld, B., Rumsey, C., and Togiti, V., “Verification and validation of a second-moment-closure model,” *AIAA Journal*, Vol. 54, No. 5, 2016, p. 1524–1541. https://doi.org/10.2514/1.j054718.

[30] Shur, M. L., Spalart, P. R., Strelets, M. K., and Travin, A. K., “A hybrid RANS-LES approach with delayed-DES and wall-modelled LES capabilities,” *International Journal of Heat and Fluid Flow*, Vol. 29, No. 6, 2008, p. 1638–1649. https://doi.org/10.1016/j.ijheatfluidflow.2008.07.001.

[31] Herr, M., Radespiel, R., and Probst, A., “Improved delayed detached eddy simulation with reynolds-stress background modelling,” *Computers &; Fluids*, Vol. 265, 2023, p. 106014. https://doi.org/10.1016/j.compfluid.2023.106014.

[32] Schwamborn, D., Gerhold, T., and Heinrich, R., “The DLR TAU-Code: Recent Applications in Research and Industry,” *ECCOMAS CFD, P. Wesseling, E. Oñate, J. Périaux (Eds), TU Delft, The Netherlands*, edited by M. Braza, A. Bottaro, and M. Thompson, 2006.

[33] Kok, J., “A high-order low-dispersion symmetry-preserving finite-volume method for compressible flow on curvilinear grids,” *Journal of Computational Physics*, Vol. 228, No. 18, 2009, p. 6811–6832. https://doi.org/10.1016/j.jcp.2009.06.015.

[34] Swanson, R., and Turkel, E., “On central-difference and upwind schemes,” *Journal of Computational Physics*, Vol. 101, No. 2, 1992, p. 292–306. https://doi.org/10.1016/0021-9991(92)90007-l.

[35] Probst, A., Löwe, J., Reuß, S., Knopp, T., and Kessler, R., “Scale-resolving simulations with a low-dissipation low-dispersion second-order scheme for unstructured flow solvers,” *AIAA Journal*, Vol. 54, No. 10, 2016, p. 2972–2987. https://doi.org/10.2514/1.j054957.

[36] Menter, F. R., “Two-equation eddy-viscosity turbulence models for engineering applications,” *AIAA Journal*, Vol. 32, No. 8, 1994, p. 1598–1605. https://doi.org/10.2514/3.12149.

[37] Gritskevich, M. S., Garbaruk, A. V., Schütze, J., and Menter, F. R., “Development of DDES and IDDES formulations for the k-$\omega$ shear stress transport model,” *Flow, Turbulence and Combustion*, Vol. 88, No. 3, 2011, p. 431–449. https://doi.org/10.1007/s10494-011-9378-4.

[38] SMAGORINSKY, J., “General circulation experiments with the primitive equations: I. The basic experiment,” *Monthly Weather Review*, Vol. 91, No. 3, 1963, p. 99–164. https://doi.org/10.1175/1520-0493(1963)091<0099:gcewtp>2.3.co;2.

[39] Menter, F. R., “Best practice: scale-resolving simulations in ANSYS CFD,” *ANSYS Germany GmbH*, Vol. 1, 2012.

[40] Spalart, P. R., and Streett, C., “Young-person’s guide to detached-eddy simulation grids,” Tech. rep., 2001.

[41] Herr, M., Probst, A., and Radespiel, R., “Grey area in embedded wall-modelled LES on a transonic nacelle-aircraft configuration,” *CEAS Aeronautical Journal*, Vol. 15, No. 1, 2023, p. 5–22. https://doi.org/10.1007/s13272-023-00664-z.

[42] Adamian, D., and Travin, A., *An efficient generator of synthetic turbulence at RANS-LES interface in embedded LES of wall-bounded and free shear flows*, Springer Berlin Heidelberg, 2011, p. 739–744. https://doi.org/10.1007/978-3-642-17884-9_94.

[43] Francois, D. G., Radespiel, R., and Probst, A., *Forced synthetic turbulence approach to stimulate resolved turbulence generation in embedded LES*, Springer International Publishing, 2015, p. 81–92. https://doi.org/10.1007/978-3-319-15141-0_6.

[44] Allmaras, S. R., and Johnson, F. T., “Modifications and clarifications for the implementation of the Spalart-Allmaras turbulence model,” *Seventh international conference on computational fluid dynamics (ICCFD7)*, Vol. 1902, Big Island, HI, 2012.

[45] Wang, L., Anderson, W. K., Nielsen, E. J., Balakumar, P., Park, M. A., Carlson, J.-R., Iyer, P. S., and Diskin, B., “Wall-modeled large-eddy simulations for high-lift configurations using FUN3D,” *AIAA SCITECH 2022 Forum*, American Institute of Aeronautics and Astronautics, 2022. https://doi.org/10.2514/6.2022-1555.

[46] Blackwell Jr, J. A., “Preliminary study of effects of Reynolds number and boundary-layer transition location on shock-induced separation,” *SPECIALISTS”MEETING ON TRANSONIC AERODYN., AGARD*, 1969.